Environmental Science & Technology

pubs.acs.org/est

Article

Interannual Variability of Air–Sea Exchange of Mercury in the Global Ocean: The "Seesaw Effect" in the Equatorial Pacific and Contributions to the Atmosphere

Shaojian Huang and Yanxu Zhang*

Cite This: *Environ. Sci. Technol.* 2021, 55, 7145–7156

Read Online

ACCESS | Metrics & More | Article Recommendations | Supporting Information

ABSTRACT: Air–sea exchange of gaseous elemental mercury (Hg(0)) is influenced by different meteorological factors and the availability of Hg in seawater. Here, we use the MITgcm ocean model to explore the interannual variability of this flux and the influence of oceanographic and atmospheric dynamics. We apply the GEOS-Chem model to further simulate the potential impact of the evasion variability on the atmospheric Hg levels. We find a latitudinal pattern in Hg(0) evasion with a relatively small variability in mid-latitudes (3.1–6.7%) and a large one in the high latitudes and Equator (>10%). Different factors dominate the patterns in the equatorial (wind speed), mid- (oceanic flow and temperature), and high-latitudinal (sea-ice, temperature, and dynamic processes) oceans. A *seesaw pattern* of Hg(0) evasion anomaly (±5–20%) in the equatorial Pacific is found from November to next January between El Niño and La Niña years, owing to the anomalies in wind speed, temperature, and vertical mixing. Higher atmospheric Hg level (2%–5%) are simulated for Hg(0) evasion fluxes with three-month lag, associated with the suppression of upwelling in the beginning of the El Niño event. Despite of the uncertainties, this study elucidates the spatial patterns of the interannual variability of the ocean Hg(0) evasion flux and its potential impact on atmospheric Hg levels.

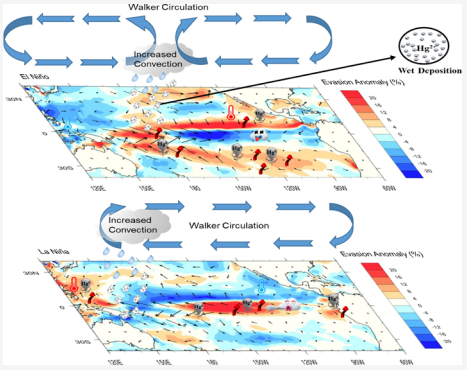

KEYWORDS: *mercury, air–sea exchange flux, interannual variability, ENSO, MITgcm, GEOS-Chem*

KEY POINTS

- The modeled global total Hg(0) evasion flux is 19 ± 0.19 Mmol/a.
- Latitudinal pattern is found with a smaller variability in the mid-latitudes (3.1%–6.7%) and a large one in the high latitudes and Equator (>10%).
- A seesaw pattern in the Equatorial Pacific is found for the evasion flux anomaly (±5%–20%) between El Niño and La Niña years.
- Higher atmospheric Hg level (2%–5%) are simulated driven by Hg(0) evasion fluxes with three-month lag after ENSO years.

1. INTRODUCTION

Mercury (Hg) is a toxic element that is ubiquitous in the environment.[1] It comes from natural sources (e.g., hydrothermal venting, volcanic eruption, and degassing), anthropogenic sources (e.g., fossil fuel combustion, metal mining, and smelting), and the re-mobilization of past-deposited sources (e.g., from terrestrial surface and ocean).[2,3] Two major chemical forms of Hg exist in the atmosphere: the elemental form (Hg(0)) that has an atmospheric lifetime of 0.5–1 year and undergoes long-range transport; and divalent form (Hg(II)) that contains a myriad of chemical forms with a shorter atmospheric lifetime (~1 week) and is deposited near source regions.[4] Other atmospheric Hg species include Hg(I) and Hg(0) bound to aerosols but with small amounts.[5,6] Before being buried in deep-sea sediment at the millennium time scale, Hg can be transported and recycled among the global atmosphere, land, and oceans.[1] Here, we focus on the air–sea exchange of Hg(0), which is the largest exchange term between different environmental compartments in the global Hg cycle.[7]

The direction of exchange is mainly upward (i.e., evasion from the ocean to the atmosphere) as the Hg(0) in the surface ocean is often supersaturated.[8−10] The air–sea exchange of Hg(0) is driven by the concentration gradients across the atmospheric and seawater interface,[11] which are influenced by a variety of physical and chemical processes such as atmospheric deposition of Hg(II) and photochemical and dark reduction/oxidation of Hg(II)/Hg(0) in the sea-

Received: January 31, 2021
Revised: April 14, 2021
Accepted: April 15, 2021
Published: April 30, 2021

water.[12−15] Soerensen et al. found a 2−4 folds greater Hg(0) fluxes in the Intertropical Convergence Zone (ITCZ) region due to the high wind speed and atmospheric Hg(II) inputted through precipitation.[16] Studies also claimed that strong convective systems reaching higher altitudes led to higher Hg concentration in precipitation comparing with weaker convective as well as strati-form systems.[17,18] In addition, dynamic factors (e.g., wind speed, ocean circulation, and diffusion) are also important for the availability of seawater Hg and the subsequent Hg(0) exchange flux.[10,11] Mason et al. discussed the possibility of upwelling to act as a source of Hg(II) driving evasion in the equatorial Pacific.[19]

In the marine boundary layer, meteorological conditions such as near-surface wind speed (U_{10}) and temperature present significantly interannual variability, which is often associated with teleconnections and oscillations of the climate system.[20,21] One example is the El Niño-Southern Oscillation (ENSO), characterized as the anomaly in sea surface temperature (SST) through the eastern Equatorial Pacific.[22] The shift of SST would cause the anomalies in sea level pressure and convection, which account for the seasonal and interannual variability of surface wind and rainfall over this region.[23,24] During the ENSO event, there are significant interannual variations in the concentrations of atmospheric trace gases such as CO_2, CO, and CH_4, indicating the varying interactions among the atmosphere, ocean, and land in the context of climate change.[25−27] It has been reported that changes of CO_2 upwelling and supply driven by ENSO can greatly influence CO_2 outgassing from central Pacific.[28] Considering the increasing trend in total Hg (THg) concentrations with depth in most oceans, a similar pattern might also apply for Hg(0) evasion.[29,30]

The variability of Hg(0) evasion might influence the atmospheric level of Hg(0) as the ocean accounts for more than one-third of the global total Hg emissions for the atmosphere.[11] Mason et al. carried out a simple model experiment and found an enhancement of the Hg(0) evasion due to mixing in the far North Atlantic.[31] Soerensen et al. attributed the atmospheric concentration differences to changes of deeper water Hg supply caused by mixing.[32] Elevated atmospheric Hg(0) concentrations were observed in an inland site when a springtime northeaster carried the outgassing from the ocean surface.[33,34] Likewise, in coastal stations such as the Mace Head, Ireland, and the Cape Point, South Africa, significant interannual variability of gaseous Hg were observed.[35−39] Slemr et al. also found an association between the variabilities of Hg concentration and the ENSO cycle.[40] We also examined the potential contribution of the interannual variability of Hg(0) evasion to the tropospheric Hg(0) levels.

2. METHODOLOGY

2.1. MITgcm Model. We use the global three-dimensional model MITgcm (Massachusetts Institute of Technology General Circulation Model) to simulate the chemistry and transport of Hg in the global ocean. Details of this model were described in Zhang et al.[41] Briefly, the model has a horizontal resolution of 1° × 1° and 50 vertical levels. The resolution is higher over the Arctic (40 km × 40 km) and the equator (0.5° latitude ×1° longitude) to better represent the ocean currents. Advection and diffusion of Hg are calculated according to the ocean state estimates from the Estimating the Circulation & Climate of the Ocean (ECCO v4) project. The model considers diapycnal (vertical) diffusion, mixed-layer turbulence closure, and simple convective adjustment.[42] The present ECCO v4 uses the third-order Direct Space Time scheme for the horizontal advection and the implicit third order upwind scheme in the vertical direction.[42] The vertical diffusion was parameterized with the GGL90 mixed layer parameterization based on the diagnostic equation of turbulent kinetic energy and closure assumptions for turbulent length scale.[43] For convective cases, the kinetic scheme from Bougeault and Lacarrere is considered as a counter-gradient term to the parameterization of the vertical flux of tracers.[44] Both the flow field and the corresponding convective mixing coefficients are used to prescribe the three-dimensional, time varying dynamic system. We thus use three parameters, vertical velocity, vertical diffusion coefficient, and convective mixing coefficient, to represent the vertical advection, diapycnal diffusion, and convective mixing processes, respectively. The meteorological data that serve as the upper boundary layer of the ocean (e.g., U_{10}, air temperature (T), precipitation, and short-wave and long-wave radiations) are from the ERA-Interim re-analysis, a climate reanalysis dataset, spanning 1992−2017.[45]

Three species of Hg in seawater including Hg(0), Hg(II), and particulate-bound mercury (Hg(P)) are considered in the model.[41] The photo- and biological-mediated oxidation and reduction reactions are considered between Hg(0) and Hg(II) following Soerensen et al.[46] One drawback of this model is the lack of temperature-dependent reaction rate coefficients. The dissolved Hg(II) can be absorbed to suspended matters to form Hg(P), and the absorbed fraction is calculated based on a constant partition coefficient and local particulate organic carbon (POC) concentrations. Hg(P) ends up in the deeper ocean by POC scavenging. The marine biogeochemical and ecological parameters (e.g., POC concentrations and sinking fluxes) are from the Darwin model.[47]

The MITgcm model takes atmospheric deposition flux and atmospheric GEM concentrations as an upper boundary condition for Hg(II) and Hg(0), respectively, and the monthly climatologically mean (from 2009 to 2011) of these data is from the GEOS-Chem model.[7] The air−sea exchange flux of Hg(0) is calculated based on the gradient between the seawater and atmosphere Hg(0) concentrations (refer to as DGM and GEM, respectively). The initial conditions of ocean Hg concentration in the MITgcm model are from Zhang et al. with each form of Hg transporting laterally and vertically by oceanic circulation and mixing. The air−sea exchange flux of Hg(0) is calculated as follows:[48−50]

$$F = K_w(DGM - GEM/H(T)) \quad (1)$$

where F represents the air−sea exchange flux, K_w is the gas exchange velocity (piston velocity), and H(T) is the dimensionless Henry's Law coefficient for Hg(0) between the atmosphere and seawater. K_w is calculated as follows:[46,51]

$$K_W = 0.31{U_{10}}^2(Sc_{Hg}/Sc_{CO2})^{-0.5} \quad (2)$$

where Sc_{Hg} and Sc_{CO2} are Schmidt numbers of Hg(0) and CO_2, respectively, which are calculated as a function of temperature.[52] $H(T)$ is from Andersson et al.:[48]

$$H(T) = \exp(-2403.3/SST + 6.92) \quad (3)$$

The model is run for 1992−2016 with initial conditions from a previous model output,[41] and the first two years are discarded as spin-up time.

https://doi.org/10.1021/acs.est.1c00691
Environ. Sci. Technol. 2021, 55, 7145−7156

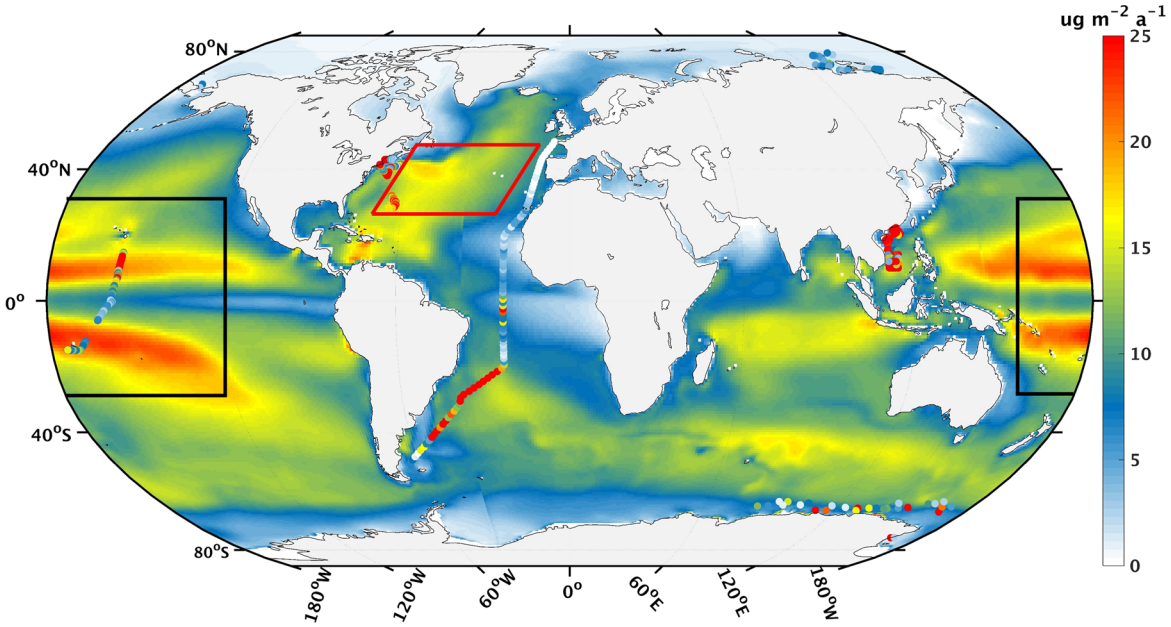

Figure 1. Modeled multiple-year mean Hg(0) fluxes in the global ocean during 1994−2016. Observed values are shown as color-coded circles.[11,16,66−69] The black box represents the region of tropical Pacific, while the North Atlantic is marked in the red box.

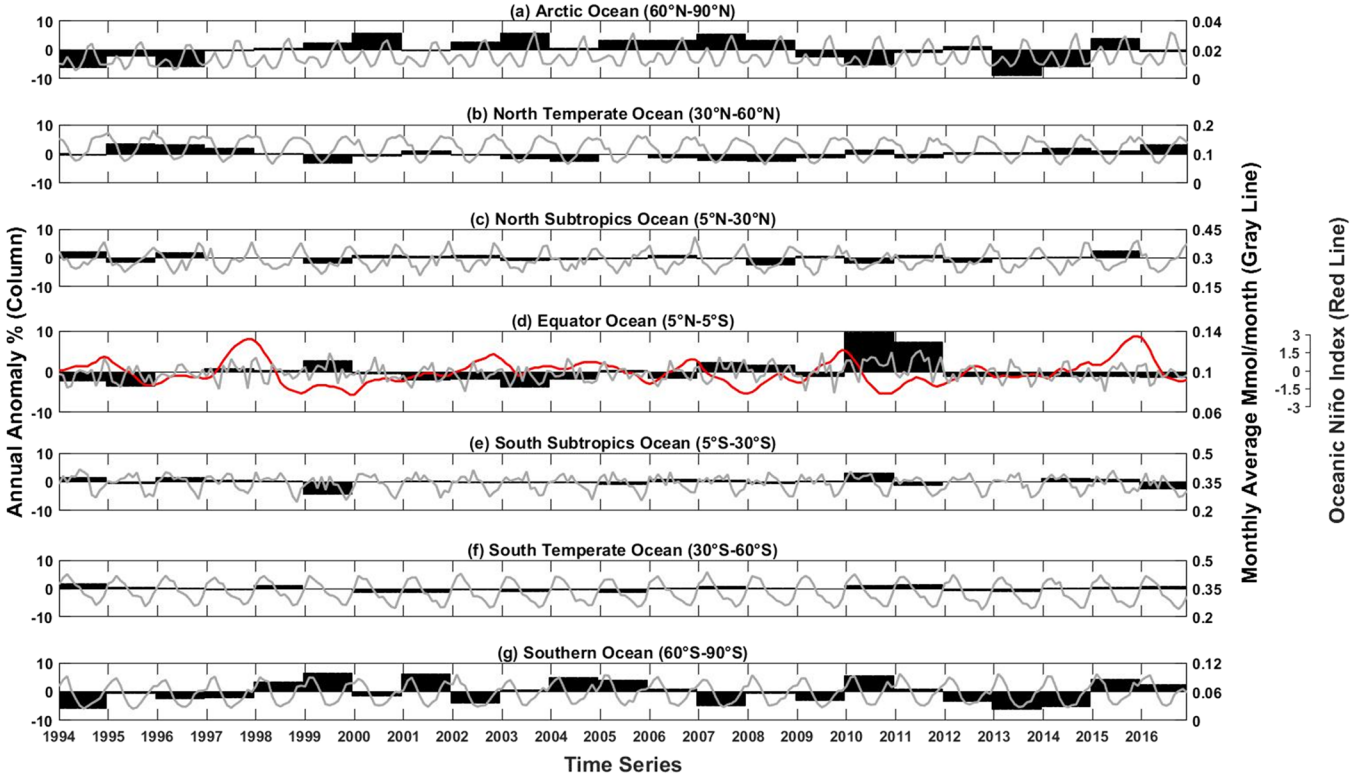

Figure 2. Interannual variability of Hg(0) evasion fluxes over different regions of the global ocean. The black shaded areas are for annual anomalies (defined as the relative difference between the annual mean and the multiple year mean from 1994−2016) (the left *y*-axis), while the gray lines are for the actual monthly average of Hg(0) evasion (the right *y*-axis). The global ocean is divided into the Arctic (90°N-60°N), northern temperate (60°N-30°N), north subtropics (30°N-5°N), equator (5°N-5°S), south subtropics (5°S-30°S), southern temperate (30°S-60°S), and the Southern Ocean (60°S-90°S). The red line represents the Oceanic Niño Index (ONI), NOAA's primary indicator for monitoring El Niño and La Niña. (https://origin.cpc.ncep.noaa.gov/) Please note the different scales used for the *y*-axes.

The model was extensively evaluated against observations in the surface ocean and water columns, and the model results agree with the observed spatial pattern and magnitudes of seawater Hg concentrations reasonably well.[41,53] We further evaluate the modeled DGM against observations (shown in the Supporting Information, Figure S1). Overall, our simulation shows comparable DGM to the observation with a similar magnitude and spatial pattern in both Pacific and Atlantic.

https://doi.org/10.1021/acs.est.1c00691
Environ. Sci. Technol. 2021, 55, 7145−7156

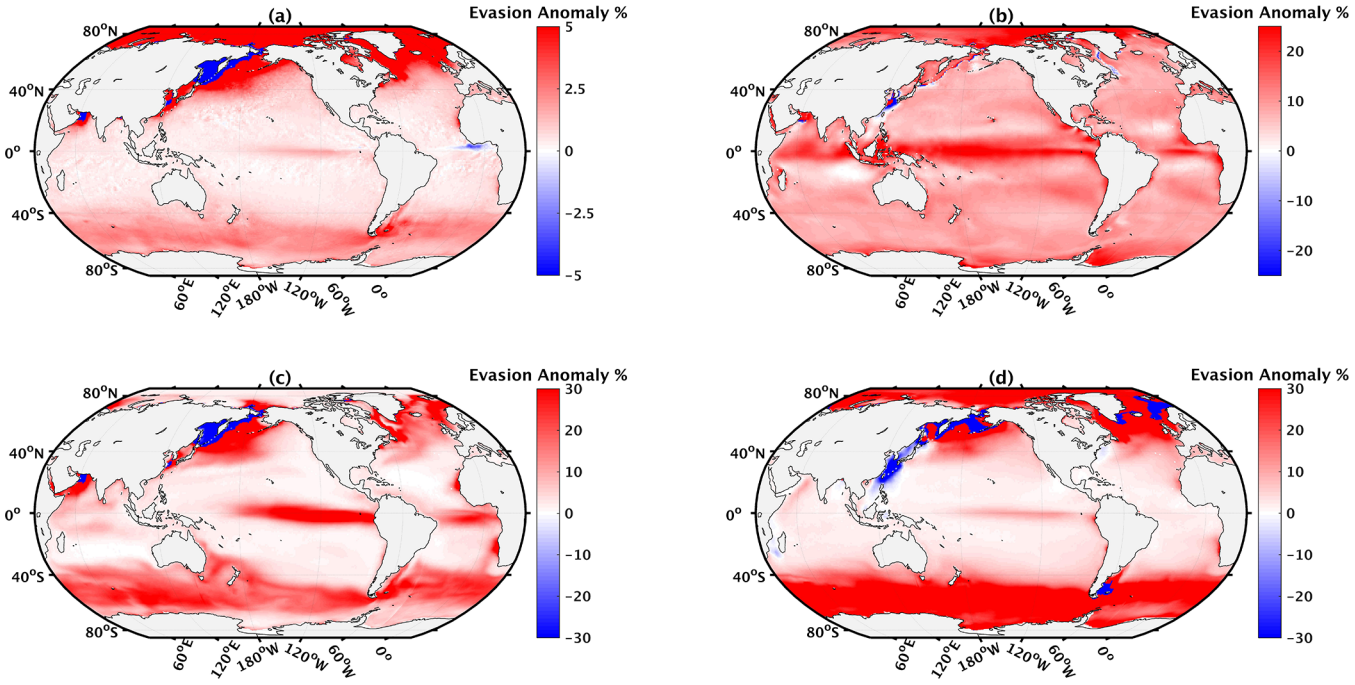

Figure 3. Sensitivity analysis of Hg(0) evasion annual anomaly to (a) SST (+1 °C), (b) U_{10} (+1 m/s), (c) vertical diffusion coefficent ($+1 \times 10^{-5}$ m^2/s), and (d) atmospheric deposition ($+1 \times 10^{-19}$ kg m^{-2} s^{-1}).

Nevertheless, the model results are slightly lower than measured DGM in the Arctic Ocean and Southern Ocean probably caused by the incomplete parameterization of the sea-ice-related processes for Hg in the MITgcm model.

2.2. GEOS-Chem Model. We use the GEOS-Chem model (version 12.2.1) (www.geos-chem.org) to simulate the impact of Hg(0) evasion flux on the atmospheric levels of Hg. This model has been widely applied to simulate the global atmospheric Hg cycle and evaluated against land-based station and cruise campaign data.[4,7,54,55] The detail of the model is described by Horowitz et al.[7] Briefly, this model is driven by assimilated meteorological data archived from the Goddard Earth Observing System (GEOS) of the NASA Global Modeling and Data Assimilation Office (GMAO), with a horizontal resolution of 4° latitude by 5° longitude and 47 vertical levels. Three atmospheric Hg tracers including Hg(0), Hg(II), and Hg(P) are simulated in this model. The model contains the oxidation of Hg(0) by Br atom and the in-cloud reduction of Hg(II). The partitioning between Hg(II) and Hg(P) is modeled following Amos et al.[56] The model also includes wet deposition of Hg(II) and Hg(P) and dry deposition of all three species. The model is driven by the anthropogenic emission inventory of Hg developed by Zhang et al.[57] The model also considers natural emissions and re-emissions from soil and snow.[58]

The monthly evasion of Hg(0) from the ocean is specified as a constant input for the GEOS-Chem model, which is from the output of the MITgcm model. The ENSO phases are divided into El Niño years and La Niña years, characterized by the 5 month running means of SST anomalies departure exceeding 0.4 °C for 6 months over the east-central equatorial Pacific [between 5°N-5°S and 170°W-120°W].[59] We average the Hg(0) evasion of the MITgcm model in four El Niño years (1997, 2004, 2009, and 2015) and four La Niña years (1996, 1999, 2007, and 2010). In addition, the non-ENSO years during 1994−2016 are also averaged to represent neutral years. The monthly evasion fluxes of Hg(0) during different phases are input to the GEOS-Chem model with other sources unchanged. The model is run with the same meteorological data (2013−2017) for each ocean evasion scenario, and the results of the last three years are analyzed. The differences among scenarios are thus solely caused by the variability of ocean evasion flux of Hg(0) but not that of the meteorology or other emission sources.

2.3. Observation Datasets. The observed Hg(0) evasion fluxes and DGM data used for model evaluation are from previous studies as illustrated in Figure 1 and Figure S1. Atmospheric Hg(0) observation datasets used in this study are from the Canadian Atmospheric Mercury Network (CAM-Net), and the European Monitoring and Evaluation Program (EMEP) networks. These observation data are compared against the calculated trends of our simulations. In addition, field data in other areas from recent studies are also discussed in this study.[38,39,60]

Decreasing trends are found for the original time series of annual Hg concentration in different observation sites.[57] We have removed the decreasing trend both in the observations and the model results before evaluating the interannual variability. We first conduct a linear regression for the atmospheric Hg(0) (or total gaseous Hg, TGM) concentrations with time as an independent variable. The calculated slope is then tested by a parametric t test for significance (α = 0.05).[61] If significant, the decreasing trends are removed from the time series by adding the product of slope and time increment to the original time series.

3. RESULTS AND DISCUSSION

3.1. Variability of Hg(0) Evasions in the Global Ocean. The modeled global total Hg(0) evasion flux is 19 ± 0.19 Mmol/a (Figure 1), similar to the magnitude of anthropogenic emissions (nearly 17 Mmol/a).[58] The net oceanic Hg evasion has been estimated in previous model studies, and our

https://doi.org/10.1021/acs.est.1c00691
Environ. Sci. Technol. 2021, 55, 7145−7156

Table 1. MLR Equation between Annual Hg(0) Evasion Fluxes and Influencing Factors in Different Ocean Regions[a]

location	MLR equation	R^2	F	P
Pacific Ocean (30°N-60°N)	NS			
Pacific Ocean (5°N-30°N)	0.589*SST	0.32	11.13	<0.01
	0.548*SST-0.394*W	0.45	10.00	<0.01
Pacific Ocean (5°S-5°N)	0.744*U_{10}	0.53	26.04	<0.01
Pacific Ocean (5°S-30°S)	0.647*Conv	0.39	15.13	<0.01
Pacific Ocean (30°S-60°S)	0.59*Conv	0.32	11.19	<0.01
	0.437*Conv-0.436*U	0.47	10.58	<0.01
Indian Ocean (5°N-20°N)	NS			
Indian Ocean (5°S-5°N)	0.545*U_{10}	0.26	8.86	<0.01
	0.691*U_{10} + 0.443*SST	0.42	8.92	<0.01
	1.091*U_{10} + 0.479*SST-0.544*U	0.56	10.14	<0.01
Indian Ocean (5°S-30°S)	−0.501*U	0.22	7.03	0.015
Indian Ocean (30°S-60°S)	−0.501*V	0.22	7.03	0.015
Atlantic Ocean (30°N-60°N)	0.804*Conv	0.63	38.41	<0.01
	0.76*Conv-0.278*T	0.69	25.98	<0.01
Atlantic Ocean (5°N-30°N)	0.516*Conv	0.23	7.63	0.012
Atlantic Ocean (5°S-5°N)	NS			
Atlantic Ocean (5°S-30°S)	NS			
Atlantic Ocean (30°S-60°S)	0.424*U	0.14	4.60	<0.01
	0.683*U + 0.608*Conv	0.43	9.34	<0.01
	0.887*U + 0.586*Conv-0.44*V	0.57	10.80	<0.01
Arctic Ocean (60°N-90°N)	0.687*SST	0.45	18.82	<0.01
	0.555*SST-0.34*W	0.53	13.28	<0.01
Southern Ocean (60°S-90°S)	0.625*V	0.36	13.46	<0.01
	0.68*V + 0.441*T	0.54	13.94	<0.01
	0.534*V + 0.66*T-0.439*U_{10}	0.65	14.66	<0.01

[a]NS: non-significant. R^2 is the determination coefficient. F stands for the Fisher ratio. P represents the significance probability level. U, V, and W are short for oceanic zonal, meridional, and vertical velocity, respectively. Conv represents the convective mixing coefficient. U_{10} is the wind speed, while T is short for air temperature.

simulation is comparable with most of the results (8.6−16.7 Mmol/a).[19,46,55,62−65] Higher Hg(0) evasion (~16 ug·m^{-2}·a^{-1}) is modeled at the tropical oceans (30°N-30°S) and decreases with latitude increases. The modeled flux is the lowest over the polar oceans due to high sea-ice coverage. Observed Hg(0) evasion fluxes remain sparse due to the requirement of simultaneous measurements of DGM, GEM, and meteorological conditions (Figure 1 and Table S1). Kuss et al. found a distinct increasing trend from 50°N to 50°S in the Atlantic Ocean, which is well captured by our simulation.[66] In a tropical Pacific cruise study, Soerensen et al. found elevated evasion fluxes over the ITCZ in the subtropical ocean but lower fluxes over the equatorial region, consistent with our model.[16] Mason et al. summarized the US GEOTRACES GP16 and GA03 data and found an increasing trend of evasion flux from east to west in both the Southeastern tropical Pacific Ocean (2.6 to 12.8 μg·m^{-2}·a^{-1}) and North Atlantic (8.0 to 18.0 μg·m^{-2}·a^{-1}).[10] (data not shown in Figure 1) Our simulations have similar westward increasing trends in the tropical Pacific (12.8 to 13.3 μg·m^{-2}·a^{-1}) and North Atlantic (10.0 to 19.2 μg·m^{-2}·a^{-1}). Our model is lower over the polar regions (0−11.8 vs 10.5−24.6 μg·m^{-2}·a^{-1}), probably caused by the incomplete representation of sea-ice Hg related processes in the model.[67,68] Coastal observations are generally high due to riverine discharge of Hg[11], which is not considered in our model.

The model bears significant uncertainties regarding the parameterization of many biogeochemical processes.[41] There are various parameterization schemes for gas exchange velocity.[50,51,70,71] Zhang et al. found similar spatial patterns for Hg(0) evasion flux for different parametrizations, and the calculated global total annual Hg(0) fluxes range from −16% to +10% compared to the Nightingale et al. scheme.[55] We find that different parameterizations result in a similar pattern in interannual variabilities (Figure S2). We also evaluate the influence of the atmospheric Hg level by using the output of different versions of GEOS-Chem.[7,16,32] The interannual variabilities are also consistent despite the magnitude varies for 20−30% (Figure S2b). Similar results are found for the vertical mixing coefficient. We thus conclude that the model uncertainty might have relatively small influence on the interannual variability of Hg(0) evasion and choose the current settings as a representative case. In addition, previous studies found a large difference between the two-film model and dynamic flux chamber results, which implies the uncertainties in measurement.[72,73] However, the general agreement between the model and observations suggests the robustness of our understandings of the spatiotemporal variability of this flux.

The global Hg(0) evasion flux varies between 18.7−19.4 Mmol/a during 1994−2016 with a distinct latitudinal pattern for its interannual variabilities (Figure 2). The model indicates that the interannual variability is relatively small in the mid-latitudes (5−60°), with the relative ranges [defined as (maximum−minimum)/mean] of annual evasion flux ranging from 3.1 to 6.7%. Slightly higher relative ranges (12.6%) are modeled in the Southern Ocean and the Arctic Ocean (±10%), consistent with Fisher et al.[36] However, a more pronounced fluctuation (13.4%) is simulated for the equatorial regions (Figure 2d, Figure S3) with higher variability for the Equatorial Pacific (19%) and Atlantic (20%) Oceans than the Equatorial Indian Ocean (9.6%). The interannual variability of Hg(0) evasion fluxes varies inversely with the Oceanic Niño Index (ONI) in equatorial regions, especially for the Equatorial Pacific. (Figure S3) This might indicate the potential impact of climate change on the Hg(0) evasion fluxes in the equator.

Substantial seasonal variability exists for Hg(0) evasion fluxes as noted by previous studies.[46,74−77] The highest Hg(0) evasion is simulated in fall and the lowest in spring in the mid-latitude oceans (Figure S4), consistent with the "mirror image-like" pattern identified by Kuss et al. for the both hemispheres.[66] Such pattern is about two months ahead in the Southern Ocean, which is attributed to the convective eddies that enhances the air−sea transfer efficiency by increasing turbulent mixing in the seawater.[78,79] In addition, the sea-ice can act as a barrier to prevent the Hg(0) from evasion,[80] which might also contribute to the lowest Hg(0) evasion in austral winter. The seasonal variability is consistent with a recent observation of atmospheric Hg(0) concentration near Amsterdam Island, a small island in the center of the southern Indian Ocean, which might indicate the great influence from ocean evasion.[38] Nevertheless, the seasonal amplitude of the

https://doi.org/10.1021/acs.est.1c00691
Environ. Sci. Technol. 2021, 55, 7145−7156

Table 2. Correlation between Annual Hg(0) Evasion Fluxes and Meteorological Parameters in Different Ocean Regions[a]

	factors								
	salinity	SST	U	V	W	Conv	U_{10}	T	sea-ice
correlation	r	r	r	r	r	r	r	r	r
Pacific Ocean									
30°N-60°N	−0.59**	−0.03	0.12	−0.03	0.10	0.28	−0.19	0.03	
5°N-30°N	−0.29	0.59**	−0.44*	0.27	−0.45*	−0.45*	0.04	−0.11	
5°S-5°N	0.22	−0.53**	0.07	−0.21	−0.06	−0.21	0.74**	−0.46*	
5°S-30°S	0.43*	−0.085	0.07	0.15	0.34	0.65**	−0.05	0.14	
30°S-60°S	−0.55**	−0.57**	−0.59**	0.37	0.23	0.59**	0.33	−0.41	
Indian Ocean									
5°N-20°N	−0.48*	−0.09	0.04	−0.22	−0.05	−0.13	0.07	0.08	
5°S-5°N	−0.13	0.22	0.15	0.31	0.18	0.04	0.55**	0.38	
5°S-30°S	0.015	−0.13	−0.50*	−0.26	0.11	0.02	−0.11	−0.23	
30°S-60°S	−0.69**	0.27	0.50*	0.003	0.35	0.17	−0.19	−0.32	
Atlantic Ocean									
30°N-60°N	0.94**	0.54**	0.04	−0.04	0.57**	0.80**	−0.04	−0.40	0.21
5°N-30°N	0.20	−0.22	−0.41	−0.44*	0.34	0.52*	−0.27	−0.21	
5°S-5°N	0.14	−0.10	−0.10	−0.35	0.40	0.23	0.21	−0.06	
5°S-30°S	−0.38	0.19	−0.06	0.17	−0.10	0.37	−0.08	0.11	
30°S-60°S	−0.57**	−0.03	0.42*	−0.15	0.02	0.32	0.01	−0.06	0.12
Southern Ocean (60°S-90°S)	0.53**	0.04	0.09	0.63**	−0.38	−0.13	−0.29	0.36	−0.22
Arctic Ocean (60°N-90°N)	−0.79**	0.69**	0.56**	0.25	−0.56**	−0.16	0.49*	0.14	−0.63**

[a]** represents the significant correlation at the level of 0.01 (bilateral); * represents the significant correlation at the level of 0.05 (bilateral).

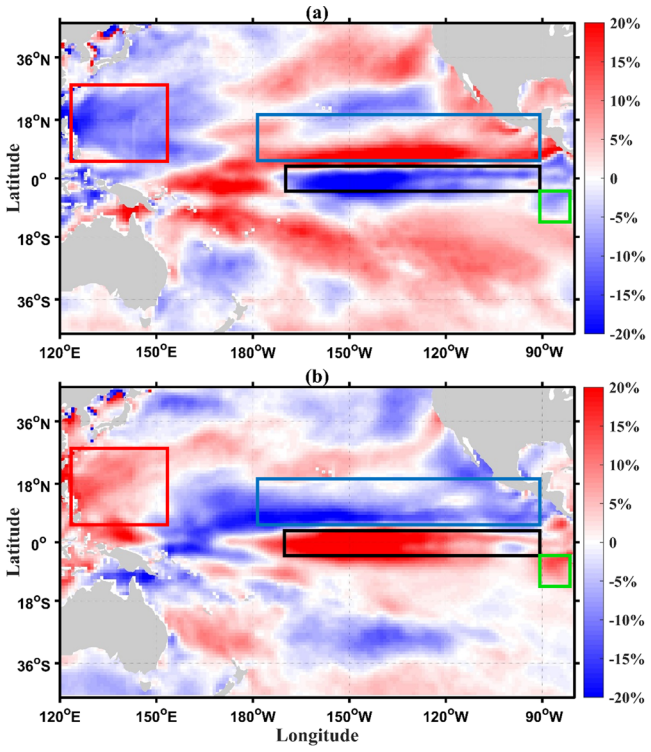

Figure 4. Hg(0) evasion anomaly compared with the average from 1994 to 2016 in November−January (NDJ) of tropical Pacific during El Niño and La Niña years. (a) Average anomaly of all El Niño events and (b) La Niña events. Black boxess represent the equatorial Pacific (5°S-5°N, 90°W-170°W). Red boxes are for the northwest Pacific (5°-30°N, 120°E-160°E). Blue boxes stand for the north subtropical Pacific (5°-20°N, 90°W-180°W)). Green boxes mark the Peruvian upwelling region (5°S-15°S, 80°W-90°W).

atmospheric Hg(0) concentration in Cape Point is smaller, with a slight decrease in austral winter. This might be associated with a weaker fluctuation from anthropogenic influence than the ocean evasion.

3.2. Influencing Factors. Large spatial variability exists for the sensitivity of Hg(0) evasion flux to different parameters (Figure 3). As we focus on the spatial variability of the influence of each variable, the increments among different variables are not consistent and should not be compared quantitatively. Details of the sensitivity simulation are provided in the Supporting Information (Page S2). Raising SST uniformly by 1 °C increases the Hg(0) evasion globally especially in the high latitude regions (1−8%) (Figure 3a), where the relatively low SST limits the evasion of Hg(0). However, increasing U_{10} (1 m/s) mainly promotes evasion fluxes in the equatorial and polar regions (Figure 3b), where the wind speed is lower than the middle-latitude ocean.[81] Doubling the vertical diffusion coefficient (Figure 3c) also significantly increases the Hg supply in upwelling regions and subsequently Hg(0) evasions (e.g., equatorial and high-latitude oceans). The impact over the downwelling regions (e.g., centers of gyres in mid-latitudes) is much smaller. This difference reflects the different vertical distributions of Hg concentrations. A general increasing trend with depth is found for Hg concentrations in the North Atlantic, central Pacific, and South Atlantic regions, but a decreasing trend is found in the subtropical North Pacific (5°N-30°N) (Table S2), the Southern, and the Arctic Ocean.[29,30,82] Increasing atmospheric deposition promotes the Hg(0) evasion the least over the mid-latitude oceans (Figure 3d), where the downwelling buries the deposited Hg that is otherwise evaded to the atmosphere.

The interannual variabilities of Hg(0) evasion reflect the simultaneous influence of multiple factors. A combination of stepwise multiple linear regression (MLR, Table 1) and correlation analysis (Table 2) is carried out to identify and quantify the relationships between Hg(0) fluxes and factors including U_{10}, T, sea-ice fraction, SST, oceanic velocity (U, V, W), and convective mixing coefficient (Conv). In addition, Table 1 also presents the contribution of each parameter to the

https://doi.org/10.1021/acs.est.1c00691
Environ. Sci. Technol. 2021, 55, 7145−7156

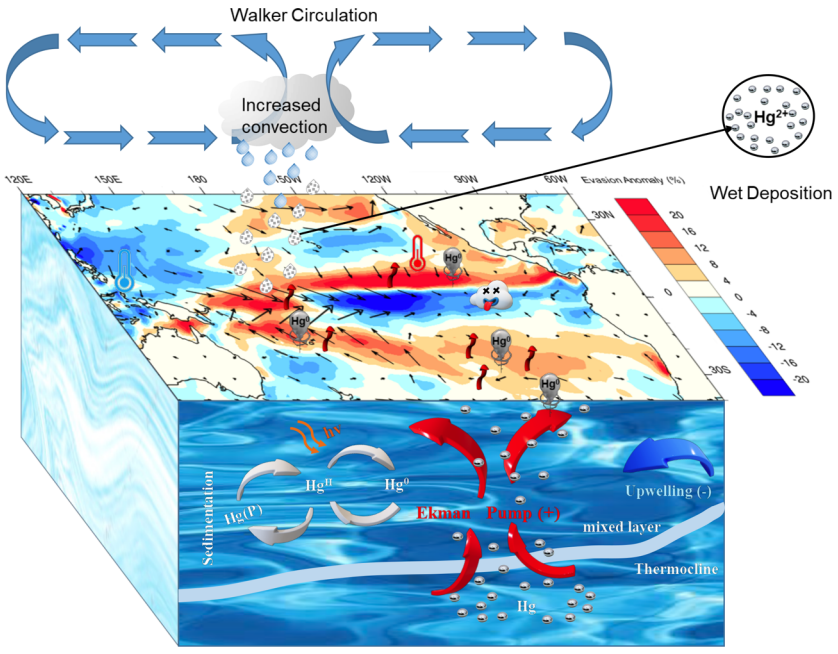

Figure 5. Concept schematic of Hg(0) evasion anomaly in the tropical Pacific during NDJ of El Niño years. Warm colors represent a positive anomaly for Hg(0) evasion flux while cold colors are for a negative anomaly. The reference vector stands for a 2 m/s velocity and wind direction. The diagram for La Niña years is in Figure S10.

Hg(0) variation by giving the MLR results with multiple variables. We find that U_{10} is the dominant factor in the equatorial oceans (except for equatorial Atlantic), consistent with the sensitivity analysis (Figure 3b). Table 1 shows that wind can explain nearly 53 and 26% of the variation in Hg(0) fluxes in equatorial Pacific and equatorial Indian Oceans, respectively. 56% of the variation is associated with U_{10}, SST, and U in equatorial Indian Ocean. The correlation coefficients with wind speed are 0.74 and 0.55 in the equatorial Pacific and Indian Oceans, respectively (Table 2), indicating the important role of U_{10} in determining the Hg(0) fluxes.

We find that flow field (U, V, W) and convective mixing is highly correlated with the Hg(0) fluxes in most of mid-low latitude oceans (5°N-60°N and 5°S-60°S) as shown in Table 2. Convective mixing is also the leading factor in MLR in the South Pacific and North Atlantic. Nearly 23−63% of the variation can be explained by this parameter in these regions (Table 1). Indeed, increasing vertical mixing (either by vertical diffusion as illustrated in Figure 3c or convective mixing) brings up Hg-rich seawater from subsurface ocean and promotes Hg(0) evasion. Similar to our sensitivity analysis in section 3.2, the correlation is also negative (−0.45) in regions with reversed vertical gradient in Hg concentrations (e.g., north subtropical Pacific Ocean). Interestingly, even though salinity has negligible impact on Hg(0) evasion, we find significant correlations between them in some basins (Table 2). Salinity reflects a combination effect of different dynamic processes including rainfall, evasion, and ocean mixing,[83−85] which also influence Hg(0) evasion.

Dynamic factors (V and U_{10}) and temperature have major contribution (about 65%) to the Hg(0) evasion variation in the Southern Ocean. (Table 1) In the Arctic Ocean, Hg(0) fluxes are mainly driven by SST (Table 1), as revealed by the sensitivity analysis in section 3.2. The flux is also anti-correlated with the sea-ice coverage (Table 2). On one hand, sea-ice blocks air−sea exchange, therefore, lower sea-ice increases Hg(0) fluxes, especially considering the high DGM under contiguous ice.[8,68,80] Lower sea-ice also increases the amount of atmospheric Hg(II) deposition entering the seawater, which would otherwise stay on top of sea-ice. On the other hand, the photoreduction of Hg(II) to Hg(0) on the ice/snow surface is suggested to be fast,[86−89] which could reduce the amount of Hg entering the seawater and the subsequent Hg(0) evasion flux. However, these effects cannot be fully evaluated in this study due to the lack of detailed Hg dynamic in sea-ice.

3.3. Seesaw Effect of Hg(0) Evasion in the Equatorial Pacific. We find that the Equatorial Pacific has the largest interannual variability for Hg(0) evasion fluxes (20%) in the global ocean due to the close air−sea interactions in this region. Indeed, tremendous heat exchange and SST anomaly occur in this region, which can cause anomalies in wind, temperature, and oceanic vertical mixing.[90,91] Variability of hydrodynamics between the eastern and western Equatorial Pacific is the essential element in developing the ENSO cycle and triggers the anomalies of zonal wind stress as well as oceanic convective mixing along the equator.[22,90] The expansion and contraction of warm water in the warm pool of the Pacific could also largely affect the atmospheric convection.[24] With an average periodicity of 3.8 years,[92] ENSO is likely to influence the interannual variability of Hg(0) evasion in the Equatorial Pacific.

Given that the El Niño and La Niña events often peak in November, December, and January (NDJ),[93] we contrast the average evasion flux in NDJ during El Niño (1997, 2004, 2009, and 2015) and La Niña (1996, 1999, 2007, and 2010) years (Figure 4). The distributions of Hg(0) evasion fluxes for individual years are shown in Figures S5 and S6. We find a prominent "seesaw pattern" for the spatial distribution of evasion anomaly between El Niño and La Niña years. During El Niño years, the evasion fluxes are 15−20% lower over the equatorial Pacific (as illustrated in the black box of Figure 4),

https://doi.org/10.1021/acs.est.1c00691
Environ. Sci. Technol. 2021, 55, 7145−7156

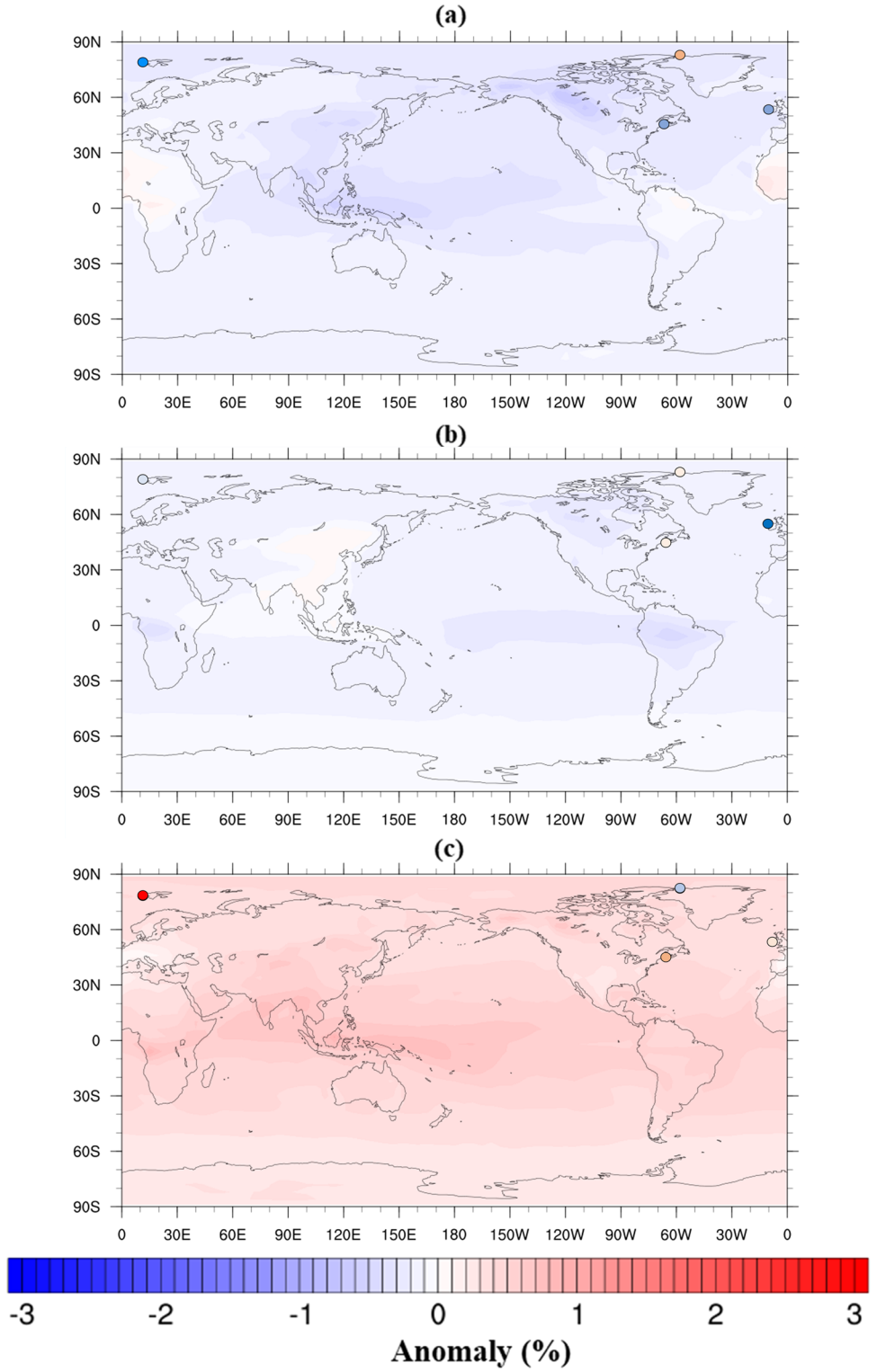

Figure 6. Percentage anomaly of atmospheric Hg concentration during (a) El Niño, (b) neutral, and (c) La Niña years compared to a multiple-year mean. Colored dots are observations in the coastal stations (Alert, Mace Head, Zeppelin, and Kejimkujik) from CAMNet (http://donnees.ec.gc.ca/data/) and EMEP sites (https://www.emep.int/).

reflecting the 15% lower wind speed in this region. The fluxes are 5−10% lower over the northwest Pacific (red box in Figure 4) and 8% lower over the Peruvian upwelling region (green box in Figure 4). On the contrary, the evasion anomalies are 10% higher over the north subtropical Pacific (blue box in Figure 4), consistent with the 10% higher wind speed. The detailed pattern varies slightly among individual years (Figures S5 and S6), but the overall patterns hold. The differences of both oceanic DGM availability and vertical velocity during the same period display similar spatial patterns (Figure S7), which indicates a potential impact of the oceanic processes on Hg(0) evasion.

https://doi.org/10.1021/acs.est.1c00691
Environ. Sci. Technol. 2021, 55, 7145−7156

Figure 5 illustrates a concept diagram for the interannual variability of Hg(0) evasion over the eastern tropical Pacific Ocean. In El Niño years, the increase of SST in the central-eastern Pacific decreases the zonal SST gradient and Walker circulation, which causes weakened or even reversed southeast trades, contributing to slower air−sea exchange velocity of Hg(0) (K_w) in the equatorial Pacific (Figure S8a).[94] On the contrary, the higher SST would also promote the gas exchange rate by increasing $H(T)$. Thus, the eastern propagation of warm pool (Figure S9a) can explain the positive evasion anomaly of Hg(0) in the north subtropical Pacific (5°-20°N, 90°W-180°W) and South Pacific. In addition, the vertical mixing also contributes to the evasion anomaly by affecting Hg availability. In the northwest Pacific (5°-30°N, 120°E-160°E), the wind divergence anomaly intensifies the vertical mixing,[95] which might bring up the less Hg-contained cold water to the surface and thus reduces the evasion (Figure S7c). The weaken Peruvian upwelling in El Niño years (Figure S7e), however, causes a negative Hg(0) evasion. A previous study found a similar decreasing pattern for CO_2 in the tropical ocean during the early stage of El Niño due to reducing upwelling.[28] While the impact of atmospheric Hg(II) deposition on Hg(0) evasion is excluded when running the model, there is no doubt that it plays an important role in the actual conditions.[16,53] Thus, we assume that the upward atmospheric motion enhances precipitation over the central or eastern Pacific, which provides more Hg(II) wet deposition to seawater for evasion. The condition during La Niña years is exactly opposite to that in El Niño years (Figure S10). The precipitation is also moved to the western Pacific, which might cause a positive anomaly of Hg(0) evasion flux there. Although both the air−sea exchange rate and ocean upwelling have great impact on the Hg(0) evasion anomaly, to quantify the exact contribution of various parameters requires further sensitivity simulations, which will be discussed in a future study.

3.4. Impact of Hg(0) Evasion on Atmospheric Levels.

Figure 6 illustrates the impact of the interannual variability of Hg(0) evasion on atmospheric Hg concentration. Despite the large regional and seasonal variability, the global annual Hg(0) evasion fluxes are relatively stable with 18.9 ± 0.1, 19.0 ± 0.1, and 18.9 ± 0.2 Mmol·a^{-1} during El Niño, La Niña, and neutral years, respectively. The resulted atmospheric Hg concentrations are thus slightly lower (−0.5%) during El Niño years and neutral years (−1%) compared with a multiple-year mean (Figure 6a,b), while higher (1%) Hg concentrations are simulated in La Niña years (Figure 6c). The spatial pattern of atmospheric Hg(0) is smoother than that of evasion flux due to the relatively long lifetime in the atmosphere.[96] Similar spatiotemporal variations are also modeled for Hg deposition (Figure S11). Generally, the atmospheric differences of Hg are statistically insignificant and other processes (i.e., volcanic emissions) might also be able to account.[4,54]

It has been reported that ENSO can also affect the meteorological conditions far from the equatorial Pacific via large-scale atmospheric teleconnections.[97−99] There is about 2−6 months lag for the ENSO-driven SST anomalies in the extratropical Pacific after the peak of ENSO. Slemr et al. have found an interannual variability of upper tropospheric (10−12 km) Hg concentrations, with a time lag of 8 ± 2 months after El Niño.[40] We find a higher simulated atmospheric Hg level (2%−5%) driven by Hg(0) evasion fluxes with a three-month lag (Figure S12). Details of the lagged simulation are provided in the Supporting Information (Page S2). A large positive anomaly (∼5%) is modeled in the equatorial Pacific Ocean for El Niño cases (Figure S12a). This phenomenon can be attributed to the increase (nearly 7%) in the ocean Hg(0) evasion for the first three months immediately after the El Niño years. (Figure S13) It indicates that the Hg(0) evasion and atmospheric Hg concentrations decrease in the early stage of El Niño (Figure 6a) and then increase after the peak of El Niño (Figure S12a), associated with the suppression of upwelling in the beginning of the El Niño event. Such a pattern is similar to that of the atmospheric CO_2 concentration found in central Pacific during a strong El Niño event.[28]

Empirical studies of the association between the variability of atmospheric Hg and the Hg(0) evasion fluxes remain sparse. Our simulations are consistent to the observations in North America and Europe, especially for those coastal stations (MHD, ALT, and ZEP and KEJ station as illustrated in Table S3) that could better represent the impact of the oceanic source. The TGM concentrations in these stations during the El Niño/neutral years are lower (−0.5 to −14.9%) compared to the multiple-year mean, while higher values (0.5 to 2.8%) are spotted in La Niña years, except for Alert (Figure 6). Recently, Bieser et al. also found a positive anomaly (nearly 25 pg·m^{-3}) of GEM concentration in a strong La Niña year after removing the influence of global gold mining and biomass burning emissions.[39] Considering the multiple influencing factors (e.g., other emission sources, atmospheric transport, and deposition), the agreement between our model and the observations suggests a potential role of ocean evasion for the interannual variability of atmospheric Hg levels.

■ ASSOCIATED CONTENT

Supporting Information

The Supporting Information is available free of charge at https://pubs.acs.org/doi/10.1021/acs.est.1c00691.

Detail description and supplementary figures for sensitivity analysis (Figure S2) and lagged simulation (Figures S12−S13); Comparison of modeled and observed DGM in different oceans (Figure S1); Interannual and seasonal variability of Hg(0) evasion fluxes (Figures S3−S4); Hg(0) evasion anomaly (Figures S5−S6), oceanic DGM availability and vertical velocity differences (Figure S7) in mature phases of El Niño and La Niña; The anomalies of wind speed and SST in mature phases of El Niño and La Niña (Figures S8−S9); Simplified schematic of Hg(0) evasion anomaly in the tropical Pacific during the mature phase of La Niña years (Figure S10); Simulated atmospheric Hg level anomalies in different ENSO schemes (Figure S11); Observation data of Hg from references and observation sites (Tables S1−S3) (PDF)

■ AUTHOR INFORMATION

Corresponding Author

Yanxu Zhang − *School of Atmospheric Sciences, Nanjing University, Nanjing 210023, China;* orcid.org/0000-0001-7770-3466; Email: zhangyx@nju.edu.cn

Author

Shaojian Huang − *School of Atmospheric Sciences, Nanjing University, Nanjing 210023, China*

Complete contact information is available at: https://pubs.acs.org/10.1021/acs.est.1c00691

Notes

The authors declare no competing financial interest.

■ ACKNOWLEDGMENTS

The authors gratefully acknowledge financial support from the National Natural Science Foundation of China (NNSFC) 41875148, Jiangsu Innovative and Entrepreneurial Talents Plan and the Collaborative Innovation Center of Climate Change, Jiangsu Province. We are grateful to the High Performance Computing Center (HPCC) of Nanjing University for doing the numerical calculations in this paper on its blade cluster system. The authors also thank the three anonymous reviewers for their constructive suggestions and comments.

■ REFERENCES

(1) Outridge, P. M.; Mason, R. P.; Wang, F.; Guerrero, S.; Heimbürger-Boavida, L. E. Updated Global and Oceanic Mercury Budgets for the United Nations Global Mercury Assessment 2018. *Environ. Sci. Technol.* **2018**, *52*, 11466−11477.

(2) Driscoll, C. T.; Mason, R. P.; Chan, H. M.; Jacob, D. J.; Pirrone, N. Mercury as a Global Pollutant: Sources, Pathways, and Effects. *Environ. Sci. Technol.* **2013**, *47*, 4967−4983.

(3) Fitzgerald, W. F.; Lamborg, C. H. Geochemistry of Mercury in the Environment. *Treatise Geochem.* **2007**, *9*, 1−47.

(4) Selin, N. E.; Jacob, D. J.; Park, R. J.; Yantosca, R. M.; Strode, S.; Jaeglé, L.; Jaffe, D. Chemical Cycling and Deposition of Atmospheric Mercury: Global Constraints from Observations. *J. Geophys. Res.: Atmos.* **2007**, *112*, D02308.

(5) Seigneur, C.; Wrobel, J.; Constantinou, E. A Chemical Kinetic Mechanism for Atmospheric Inorganic Mercury. *Environ. Sci. Technol.* **1994**, *28*, 1589−1597.

(6) Fu, X.; Zhang, H.; Liu, C.; Zhang, H.; Lin, C.-J.; Feng, X. Significant Seasonal Variations in Isotopic Composition of Atmospheric Total Gaseous Mercury at Forest Sites in China Caused by Vegetation and Mercury Sources. *Environ. Sci. Technol.* **2019**, *53*, 13748−13756.

(7) Horowitz, H. M.; Jacob, D. J.; Zhang, Y.; Dibble, T. S.; Slemr, F.; Amos, H. M.; Schmidt, J. A.; Corbitt, E. S.; Marais, E. A.; Sunderland, E. M. A New Mechanism for Atmospheric Mercury Redox Chemistry: Implications for the Global Mercury Budget. *Atmos. Chem. Phys.* **2017**, *17*, 6353−6371.

(8) Andersson, M. E.; Sommar, J.; Gårdfeldt, K.; Lindqvist, O. Enhanced Concentrations of Dissolved Gaseous Mercury in the Surface Waters of the Arctic Ocean. *Mar. Chem.* **2008**, *110*, 190−194.

(9) Mason, R. P.; Lawson, N. M.; Sheu, G.-R. Mercury in the Atlantic Ocean: Factors Controlling Air−Sea Exchange of Mercury and Its Distribution in the Upper Waters. *Deep Sea Res., Part II* **2001**, *48*, 2829−2853.

(10) Mason, R. P.; Hammerschmidt, C. R.; Lamborg, C. H.; Bowman, K. L.; Swarr, G. J.; Shelley, R. U. The Air-Sea Exchange of Mercury in the Low Latitude Pacific and Atlantic Oceans. *Deep-Sea Res., Part A* **2017**, *122*, 17−28.

(11) Soerensen, A. L.; Mason, R. P.; Balcom, P. H.; Sunderland, E. M. Drivers of Surface Ocean Mercury Concentrations and Air-Sea Exchange in the West Atlantic Ocean. *Environ. Sci. Technol.* **2013**, *47*, 7757−7765.

(12) Costa, M.; Liss, P. S. Photoreduction of Mercury in Sea Water and Its Possible Implications for Hg0 Air−Sea Fluxes. *Mar. Chem.* **1999**, *68*, 87−95.

(13) Gårdfeldt, K.; Sommar, J.; Strömberg, D.; Feng, X. Oxidation of Atomic Mercury by Hydroxyl Radicals and Photoinduced Decomposition of Methylmercury in the Aqueous Phase. *Atmos. Environ.* **2001**, *35*, 3039−3047.

(14) Andersson, M. E.; Sommar, J.; Gårdfeldt, K.; Jutterström, S. Air−Sea Exchange of Volatile Mercury in the North Atlantic Ocean. *Mar. Chem.* **2011**, *125*, 1−7.

(15) Ci, Z.; Zhang, X.; Yin, Y.; Chen, J.; Wang, S. Mercury Redox Chemistry in Waters of the Eastern Asian Seas: From Polluted Coast to Clean Open Ocean. *Environ. Sci. Technol.* **2016**, *50*, 2371−2380.

(16) Soerensen, A. L.; Mason, R. P.; Balcom, P. H.; Jacob, D. J.; Zhang, Y.; Kuss, J.; Sunderland, E. M. Elemental Mercury Concentrations and Fluxes in the Tropical Atmosphere and Ocean. *Environ. Sci. Technol.* **2014**, *48*, 11312−11319.

(17) Zhang, Y.; Jaeglé, L.; Van Donkelaar, A.; Martin, R. V.; Holmes, C. D.; Amos, H. M.; Wang, Q.; Talbot, R.; Artz, R.; Brooks, S.; Luke, W.; Holsen, T. M.; Felton, D.; Miller, E. K.; Perry, K. D.; Schmeltz, D.; Steffen, A.; Tordon, R.; Weiss-Penzias, P.; Zsolway, R. Nested-Grid Simulation of Mercury over North America. *Atmos. Chem. Phys.* **2012**, *12*, 6095−6111.

(18) Holmes, C. D.; Krishnamurthy, N. P.; Caffrey, J. M.; Landing, W. M.; Edgerton, E. S.; Knapp, K. R.; Nair, U. S. Thunderstorms Increase Mercury Wet Deposition. *Environ. Sci. Technol.* **2016**, *50*, 9343−9350.

(19) Mason, R. P.; Fitzgerald, W. F.; Morel, F. M. M. The Biogeochemical Cycling of Elemental Mercury: Anthropogenic Influences. *Geochim. Cosmochim. Acta* **1994**, *58*, 3191−3198.

(20) Grimm, A. M.; Natori, A. A. Climate Change and Interannual Variability of Precipitation in South America. *Geophys. Res. Lett.* **2006**, *33*, 1−5.

(21) Romero-Centeno, R.; Zavala-Hidalgo, J.; Gallegos, A.; O'Brien, J. J. Isthmus of Tehuantepec Wind Climatology and ENSO Signal. *J. Clim.* **2003**, *16*, 2628−2639.

(22) Guilderson, T. P.; Schrag, D. P. Abrupt Shift in Subsurface Temperatures in the Tropical Pacific Associated with Changes in El Nino. *Science* **1998**, *281*, 240−243.

(23) Janowiak, J. E.; Arkin, P. A. Rainfall Variations in the Tropics during 1986-1989, as Estimated from Observations of Cloud-Top Temperature. *J. Geophys. Res.* **1991**, *96*, 3359−3373.

(24) Wang, C.; Enfield, D. B. The Tropical Western Hemisphere Warm Pool. *Geophys. Res. Lett.* **2001**, *28*, 1635−1638.

(25) Monks, S. A.; Arnold, S. R.; Chipperfield, M. P. Evidence for El Niño−Southern Oscillation (ENSO) Influence on Arctic CO Interannual Variability through Biomass Burning Emissions. *Geophys. Res. Lett.* **2012**, *39*, L14804.

(26) Malhi, Y.; Rowland, L.; Aragão, L. E. O. C.; Fisher, R. A. New Insights into the Variability of the Tropical Land Carbon Cycle from the El Niño of 2015/2016. *Philos. Trans. R. Soc., B* **2018**, *373*, 20170298.

(27) Rowlinson, M. J.; Rap, A.; Arnold, S. R.; Pope, R. J.; Chipperfield, M. P.; McNorton, J.; Forster, P.; Gordon, H.; Pringle, K. J.; Feng, W.; Kerridge, B. J.; Latter, B. L.; Siddans, R. Impact of El Niño−Southern Oscillation on the Interannual Variability of Methane and Tropospheric Ozone. *Atmos. Chem. Phys.* **2019**, *19*, 8669−8686.

(28) Chatterjee, A.; Gierach, M. M.; Sutton, A. J.; Feely, R. A.; Crisp, D.; Eldering, A.; Gunson, M. R.; O'Dell, C. W.; Stephens, B. B.; Schimel, D. S. Influence of El Niño on Atmospheric CO_2 over the Tropical Pacific Ocean: Findings from NASA's OCO-2 Mission. *Science* **2017**, *358*, eaam5776.

(29) Munson, K. M.; Lamborg, C. H.; Swarr, G. J.; Saito, M. A. Mercury Species Concentrations and Fluxes in the Central Tropical Pacific Ocean. *Global Biogeochem. Cycles* **2015**, *29*, 656−676.

(30) Bowman, K. L.; Hammerschmidt, C. R.; Lamborg, C. H.; Swarr, G. Mercury in the North Atlantic Ocean: The U.S. GEOTRACES Zonal and Meridional Sections. *Deep Sea Res., Part II* **2015**, *116*, 251−261.

(31) Mason, R. P.; Rolfhus, K. R.; Fitzgerald, W. F. Mercury in the North Atlantic. *Mar. Chem.* **1998**, *61*, 37−53.

(32) Soerensen, A. L.; Jacob, D. J.; Streets, D. G.; Witt, M. L. I.; Ebinghaus, R.; Mason, R. P.; Andersson, M.; Sunderland, E. M. Multi-Decadal Decline of Mercury in the North Atlantic Atmosphere Explained by Changing Subsurface Seawater Concentrations. *Geophys. Res. Lett.* **2012**, *39*, L21810.

(33) Malcolm, E. G.; Keeler, G. J.; Landis, M. S. The Effects of the Coastal Environment on the Atmospheric Mercury Cycle. *J. Geophys. Res.: Atmos.* **2003**, *108*, 4357.

https://doi.org/10.1021/acs.est.1c00691
Environ. Sci. Technol. 2021, 55, 7145−7156

(34) Sigler, J. M.; Mao, H.; Talbot, R. Gaseous Elemental and Reactive Mercury in Southern New Hampshire. *Atmos. Chem. Phys.* **2009**, *9*, 1929−1942.
(35) Ebinghaus, R.; Jennings, S. G.; Kock, H. H.; Derwent, R. G.; Manning, A. J.; Spain, T. G. Decreasing Trends in Total Gaseous Mercury Observations in Baseline Air at Mace Head, Ireland from 1996 to 2009. *Atmos. Environ.* **2011**, *45*, 3475−3480.
(36) Fisher, J. A.; Jacob, D. J.; Soerensen, A. L.; Amos, H. M.; Corbitt, E. S.; Streets, D. G.; Wang, Q.; Yantosca, R. M.; Sunderland, E. M. Factors Driving Mercury Variability in the Arctic Atmosphere and Ocean over the Past 30 Years. *Global Biogeochem. Cycles* **2013**, *27*, 1226−1235.
(37) Slemr, F.; Brunke, E. G.; Labuschagne, C.; Ebinghaus, R. Total Gaseous Mercury Concentrations at the Cape Point GAW Station and Their Seasonality. *Geophys. Res. Lett.* **2008**, *35*, L11807.
(38) Slemr, F.; Martin, L.; Labuschagne, C.; Mkololo, T.; Angot, H.; Magand, O.; Dommergue, A.; Garat, P.; Ramonet, M.; Bieser, J. Atmospheric Mercury in the Southern Hemisphere − Part 1: Trend and Inter-Annual Variations in Atmospheric Mercury at Cape Point, South Africa, in 2007−2017, and on Amsterdam Island in 2012−2017. *Atmos. Chem. Phys.* **2020**, *20*, 7683−7692.
(39) Bieser, J.; Angot, H.; Slemr, F.; Martin, L. Atmospheric Mercury in the Southern Hemisphere - Part 2: Source Apportionment Analysis at Cape Point Station, South Africa. *Atmos. Chem. Phys.* **2020**, *20*, 10427−10439.
(40) Slemr, F.; Brenninkmeijer, C. A.; Rauthe-Schöch, A.; Weigelt, A.; Ebinghaus, R.; Brunke, E.-G.; Martin, L.; Spain, T. G.; O'Doherty, S. El Niño−Southern Oscillation Influence on Tropospheric Mercury Concentrations. *Geophys. Res. Lett.* **2016**, *43*, 1766−1771.
(41) Zhang, Y.; Soerensen, A. L.; Schartup, A. T.; Sunderland, E. M. A Global Model for Methylmercury Formation and Uptake at the Base of Marine Food Webs. *Global Biogeochem. Cycles* **2020**, *34*, e2019GB006348.
(42) Forget, G.; Campin, J.-M.; Heimbach, P.; Hill, C. N.; Ponte, R. M.; Wunsch, C. ECCO Version 4: An Integrated Framework for Non-Linear Inverse Modeling and Global Ocean State Estimation. *Geosci. Model Dev.* **2015**, *8*, 3071−3104.
(43) Gaspar, P.; Grégoris, Y.; Lefevre, J.-M. A Simple Eddy Kinetic Energy Model for Simulations of the Oceanic Vertical Mixing: Tests at Station Papa and Long-Term Upper Ocean Study Site. *J. Geophys. Res.: Planets* **1990**, *95*, 16179−16193.
(44) Bougeault, P.; Lacarrere, P. Parameterization of Orography-Induced Turbulence in a Mesobeta–Scale Model. *Mon. Weather Rev.* **1989**, *117*, 1872−1890.
(45) Dee, D. P.; Uppala, S. M.; Simmons, A. J.; Berrisford, P.; Poli, P.; Kobayashi, S.; Andrae, U.; Balmaseda, M. A.; Balsamo, G.; Bauer, P.; Bechtold, P.; Beljaars, A. C. M.; van de Berg, L.; Bidlot, J.; Bormann, N.; Delsol, C.; Dragani, R.; Fuentes, M.; Geer, A. J.; Haimberger, L.; Healy, S. B.; Hersbach, H.; Hólm, E. V.; Isaksen, L.; Kållberg, P.; Köhler, M.; Matricardi, M.; McNally, A. P.; Monge-Sanz, B. M.; Morcrette, J.-J.; Park, B.-K.; Peubey, C.; de Rosnay, P.; Tavolato, C.; Thépaut, J. N.; Vitart, F. The ERA-Interim Reanalysis: Configuration and Performance of the Data Assimilation System. *Q. J. R. Meteorol. Soc.* **2011**, *137*, 553−597.
(46) Soerensen, A. L.; Sunderland, E. M.; Holmes, C. D.; Jacob, D. J.; Yantosca, R. M.; Skov, H.; Christensen, J. H.; Strode, S. A.; Mason, R. P. An Improved Global Model for Air-Sea Exchange of Mercury: High Concentrations over the North Atlantic. *Environ. Sci. Technol.* **2010**, *44*, 8574−8580.
(47) Dutkiewicz, S.; Follows, M. J.; Bragg, J. G. Modeling the Coupling of Ocean Ecology and Biogeochemistry. *Global Biogeochem. Cycles* **2009**, *23*, 1−15.
(48) Andersson, M. E.; Gårdfeldt, K.; Wängberg, I.; Strömberg, D. Determination of Henry's Law Constant for Elemental Mercury. *Chemosphere* **2008**, *73*, 587−592.
(49) Fu, X.; Feng, X.; Zhang, G.; Xu, W.; Li, X.; Yao, H.; Liang, P.; Li, J.; Sommar, J.; Yin, R. S.; Liu, N. Mercury in the Marine Boundary Layer and Seawater of the South China Sea: Concentrations, Sea/Air Flux, and Implication for Land Outflow. *J. Geophys. Res.: Atmos.* **2010**, *115*, 1−11.
(50) Wanninkhof, R. Relationship between Wind Speed and Gas Exchange over the Ocean. *J. Geophys. Res.* **1992**, *97*, 7373−7382.
(51) Nightingale, P. D.; Malin, G.; Law, C. S.; Watson, A. J.; Liss, P. S.; Liddicoat, M. I.; Boutin, J.; Upstill-Goddard, R. C. In Situ Evaluation of Air-Sea Gas Exchange Parameterizations Using Novel Conservative and Volatile Tracers. *Global Biogeochem. Cycles* **2000**, *14*, 373−387.
(52) Poissant, L.; Amyot, M.; Pilote, M.; Lean, D. Mercury Water−Air Exchange over the Upper St. Lawrence River and Lake Ontario. *Environ. Sci. Technol.* **2000**, *34*, 3069−3078.
(53) Zhang, Y.; Jacob, D. J.; Dutkiewicz, S.; Amos, H. M.; Long, M. S.; Sunderland, E. M. Biogeochemical Drivers of the Fate of Riverine Mercury Discharged to the Global and Arctic Oceans. *Global Biogeochem. Cycles* **2015**, *29*, 854−864.
(54) Holmes, C. D.; Jacob, D. J.; Corbitt, E. S.; Mao, J.; Yang, X.; Talbot, R.; Slemr, F. Global Atmospheric Model for Mercury Including Oxidation by Bromine Atoms. *Atmos. Chem. Phys.* **2010**, *10*, 12037−12057.
(55) Zhang, Y.; Horowitz, H.; Wang, J.; Xie, Z.; Kuss, J.; Soerensen, A. L. A Coupled Global Atmosphere-Ocean Model for Air-Sea Exchange of Mercury: Insights into Wet Deposition and Atmospheric Redox Chemistry. *Environ. Sci. Technol.* **2019**, *53*, 5052−5061.
(56) Amos, H. M.; Jacob, D. J.; Holmes, C. D.; Fisher, J. A.; Wang, Q.; Yantosca, R. M.; Corbitt, E. S.; Galarneau, E.; Rutter, A. P.; Gustin, M. S.; Steffen, A.; Schauer, J. J.; Graydon, J. A.; Louis, V. L. S.; Talbot, R. W.; Edgerton, E. S.; Zhang, Y.; Sunderland, E. M. Gas-Particle Partitioning of Atmospheric Hg(II) and Its Effect on Global Mercury Deposition. *Atmos. Chem. Phys.* **2012**, *12*, 591−603.
(57) Zhang, Y.; Jacob, D. J.; Horowitz, H. M.; Chen, L.; Amos, H. M.; Krabbenhoft, D. P.; Slemr, F.; St. Louis, V. L.; Sunderland, E. M. Observed Decrease in Atmospheric Mercury Explained by Global Decline in Anthropogenic Emissions. *Proc. Natl. Acad. Sci. U. S. A.* **2016**, *113*, 526−531.
(58) Selin, N. E.; Jacob, D. J.; Yantosca, R. M.; Strode, S.; Jaeglé, L.; Sunderland, E. M. Global 3-D Land-Ocean-Atmosphere Model for Mercury: Present-Day versus Preindustrial Cycles and Anthropogenic Enrichment Factors for Deposition. *Global Biogeochem. Cycles* **2008**, *22*, DOI: 10.1029/2007GB003040
(59) Trenberth, K. E. The Definition of El Niño. *Bull. Am. Meteorol. Soc.* **1997**, *78*, 2771−2777.
(60) Howard, D.; Nelson, P. F.; Edwards, G. C.; Morrison, A. L.; Fisher, J. A.; Ward, J.; Harnwell, J.; van der Schoot, M.; Atkinson, B.; Chambers, S. D.; Griffiths, A. D.; Werczynski, S.; Williams, A. G. Atmospheric mercury in the Southern Hemisphere tropics: seasonal and diurnal variations and influence of inter-hemispheric transport. *Atmos. Chem. Phys.* **2017**, *17*, 11623−11636.
(61) Xu, C.; Gong, L.; Jiang, T.; Chen, D.; Singh, V. P. Analysis of Spatial Distribution and Temporal Trend of Reference Evapotranspiration and Pan Evaporation in Changjiang (Yangtze River) Catchment. *J. Hydrol.* **2006**, *327*, 81−93.
(62) Lamborg, C. H.; Fitzgerald, W. F.; O'Donnell, J.; Torgersen, T. A Non-Steady-State Compartmental Model of Global-Scale Mercury Biogeochemistry with Interhemispheric Atmospheric Gradients. *Geochim. Cosmochim. Acta* **2002**, *66*, 1105−1118.
(63) Mason, R. P.; Sheu, G.-R. Role of the Ocean in the Global Mercury Cycle. *Global Biogeochem. Cycles* **2002**, *16*, 40-1−40-14.
(64) Kawai, T.; Sakurai, T.; Suzuki, N. Application of a New Dynamic 3-D Model to Investigate Human Impacts on the Fate of Mercury in the Global Ocean. *Environ. Model. Softw.* **2020**, *124*, 104599.
(65) Zhang, Y.; Jaeglé, L.; Thompson, L. A.; Streets, D. G. Six Centuries of Changing Oceanic Mercury. *Global Biogeochem. Cycles* **2014**, *28*, 1251−1261.
(66) Kuss, J.; Zülicke, C.; Pohl, C.; Schneider, B. Atlantic Mercury Emission Determined from Continuous Analysis of the Elemental Mercury Sea-Air Concentration Difference within Transects between 50°N and 50°S. *Global Biogeochem. Cycles* **2011**, *25*, 1−9.

(67) Kalinchuk, V. V.; Lopatnikov, E. A.; Astakhov, A. S.; Ivanov, M. V.; Hu, L. Distribution of Atmospheric Gaseous Elemental Mercury (Hg(0)) from the Sea of Japan to the Arctic, and Hg(0) Evasion Fluxes in the Eastern Arctic Seas: Results from a Joint Russian-Chinese Cruise in Fall 2018. *Sci. Total Environ.* **2021**, *753*, 142003.
(68) Wang, J.; Xie, Z.; Wang, F.; Kang, H. Gaseous Elemental Mercury in the Marine Boundary Layer and Air-Sea Flux in the Southern Ocean in Austral Summer. *Sci. Total Environ.* **2017**, *603-604*, 510−518.
(69) Wang, C.; Wang, Z.; Hui, F.; Zhang, X. Speciated Atmospheric Mercury and Sea−Air Exchange of Gaseous Mercury in the South China Sea. *Atmos. Chem. Phys.* **2019**, *19*, 10111−10127.
(70) McGillis, W. R.; Edson, J. B.; Hare, J. E.; Fairall, C. W. Direct Covariance Air-Sea CO_2 Fluxes. *J. Geophys. Res.* **2001**, *106*, 16729−16745.
(71) Wanninkhof, R.; McGillis, W. R. A Cubic Relationship between Air-Sea CO_2 Exchange and Wind Speed. *Geophys. Res. Lett.* **1999**, *26*, 1889−1892.
(72) Zhang, H. H.; Poissant, L.; Xu, X.; Pilote, M.; Beauvais, C.; Amyot, M.; Garcia, E.; Laroulandie, J. Air-Water Gas Exchange of Mercury in the Bay Saint François Wetlands: Observation and Model Parameterization. *J. Geophys. Res.: Atmos.* **2006**, *111*, D17307.
(73) Fu, X.; Feng, X.; Yin, R.; Zhang, H. Diurnal Variations of Total Mercury, Reactive Mercury, and Dissolved Gaseous Mercury Concentrations and Water/Air Mercury Flux in Warm and Cold Seasons from Freshwaters of Southwestern China. *Environ. Toxicol. Chem.* **2013**, *32*, 2256−2265.
(74) Andersson, M. E.; Gårdfeldt, K.; Wängberg, I.; Sprovieri, F.; Pirrone, N.; Lindqvist, O. Seasonal and Daily Variation of Mercury Evasion at Coastal and off Shore Sites from the Mediterranean Sea. *Mar. Chem.* **2007**, *104*, 214−226.
(75) Song, S.; Selin, N. E.; Soerensen, A. L.; Angot, H.; Artz, R.; Brooks, S.; Brunke, E.-G.; Conley, G.; Dommergue, A.; Ebinghaus, R.; Holsen, T. M.; Jaffe, D. A.; Kang, S.; Kelley, P.; Luke, W. T.; Magand, O.; Marumoto, K.; Pfaffhuber, K. A.; Ren, X.; Sheu, G. R.; Slemr, F.; Warneke, T.; Weigelt, A.; Weiss-Penzias, P.; Wip, D. C.; Zhang, Q. Top-down Constraints on Atmospheric Mercury Emissions and Implications for Global Biogeochemical Cycling. *Atmos. Chem. Phys.* **2015**, *15*, 7103−7125.
(76) Strode, S. A.; Jaeglé, L.; Selin, N. E.; Jacob, D. J.; Park, R. J.; Yantosca, R. M.; Mason, R. P.; Slemr, F. Air-Sea Exchange in the Global Mercury Cycle. *Global Biogeochem. Cycles* **2007**, *21*, 1−12.
(77) Weigelt, A.; Ebinghaus, R.; Manning, A. J.; Derwent, R. G.; Simmonds, P. G.; Spain, T. G.; Jennings, S. G.; Slemr, F. Analysis and Interpretation of 18 Years of Mercury Observations since 1996 at Mace Head, Ireland. *Atmos. Environ.* **2015**, *100*, 85−93.
(78) Rutgersson, A.; Smedman, A.; Sahlée, E. Oceanic Convective Mixing and the Impact on Air-Sea Gas Transfer Velocity. *Geophys. Res. Lett.* **2011**, *38*, L02602.
(79) Rutgersson, A.; Smedman, A. Enhanced Air−Sea CO2 Transfer Due to Water-Side Convection. *J. Mar. Syst.* **2010**, *80*, 125−134.
(80) DiMento, B. P.; Mason, R. P.; Brooks, S.; Moore, C. The Impact of Sea Ice on the Air-Sea Exchange of Mercury in the Arctic Ocean. *Deep-Sea Res., Part A* **2019**, *144*, 28−38.
(81) Hu, Y.; Stamnes, K.; Vaughan, M.; Pelon, J.; Weimer, C.; Wu, D.; Cisewski, M.; Sun, W.; Yang, P.; Lin, B.; Omar, A.; Flittner, D.; Hostetler, C.; Trepte, C.; Winker, D.; Gibson, G.; Santa-Maria, M. Sea Surface Wind Speed Estimation from Space-Based Lidar Measurements. *Atmos. Chem. Phys.* **2008**, *8*, 3593−3601.
(82) Bratkič, A.; Vahčič, M.; Kotnik, J.; Obu Vazner, K.; Begu, E.; Woodward, E. M. S.; Horvat, M. Mercury Presence and Speciation in the South Atlantic Ocean along the 40°S Transect. *Global Biogeochem. Cycles* **2016**, *30*, 105−119.
(83) Helm, K. P.; Bindoff, N. L.; Church, J. A. Changes in the Global Hydrological-Cycle Inferred from Ocean Salinity. *Geophys. Res. Lett.* **2010**, *37*, L18701.
(84) Hasson, A. E. A.; Delcroix, T.; Dussin, R. An Assessment of the Mixed Layer Salinity Budget in the Tropical Pacific Ocean. Observations and Modelling (1990−2009). *Ocean Dyn.* **2013**, *63*, 179−194.
(85) Liu, C.; Liang, X.; Ponte, R. M.; Vinogradova, N.; Wang, O. Vertical Redistribution of Salt and Layered Changes in Global Ocean Salinity. *Nat. Commun.* **2019**, *10*, 3445.
(86) Dommergue, A.; Bahlmann, E.; Ebinghaus, R.; Ferrari, C.; Boutron, C. Laboratory Simulation of Hg0 Emissions from a Snowpack. *Anal. Bioanal. Chem.* **2007**, *388*, 319−327.
(87) Johnson, K. P.; Blum, J. D.; Keeler, G. J.; Douglas, T. A. Investigation of the Deposition and Emission of Mercury in Arctic Snow during an Atmospheric Mercury Depletion Event. *J. Geophys. Res. Atmos.* **2008**, *113*, D17304.
(88) Kirk, J. L.; St. Louis, V. L.; Sharp, M. J. Rapid Reduction and Reemission of Mercury Deposited into Snowpacks during Atmospheric Mercury Depletion Events at Churchill, Manitoba, Canada. *Environ. Sci. Technol.* **2006**, *40*, 7590−7596.
(89) Sherman, L. S.; Blum, J. D.; Johnson, K. P.; Keeler, G. J.; Barres, J. A.; Douglas, T. A. Mass-Independent Fractionation of Mercury Isotopes in Arctic Snow Driven by Sunlight. *Nat. Geosci.* **2010**, *3*, 173−177.
(90) Vimont, D. J.; Wallace, J. M.; Battisti, D. S. The Seasonal Footprinting Mechanism in the Pacific: Implications for ENSO. *J. Clim.* **2003**, *16*, 2668−2675.
(91) Wallace, J. M.; Mitchell, T. P.; Deser, C. The Influence of Sea-Surface Temperature on Surface Wind in the Eastern Equatorial Pacific: Seasonal and Interannual Variability. *J. Clim.* **1989**, *2*, 1492−1499.
(92) Quinn, W. H.; Neal, V. T.; Antunez De Mayolo, S. E. El Niño Occurrences over the Past Four and a Half Centuries. *J. Geophys. Res.: Planets* **1987**, *92*, 14449−14461.
(93) An, S.-I.; Wang, B. Mechanisms of Locking of the El Niño and La Niña Mature Phases to Boreal Winter. *J. Clim.* **2001**, *14*, 2164−2176.
(94) Cess, R. D.; Zhang, M.; Wang, P. H.; Wielicki, B. A. Cloud structure anomalies over the tropical Pacific during the 1997/98 El Niño. *Geophys. Res. Lett.* **2001**, *28*, 4547−4550.
(95) Chang, Y.-T.; Du, L.; Zhang, S.-W.; Huang, P.-F. Sea Level Variations in the Tropical Pacific Ocean during Two Types of Recent El Niño Events. *Glob. Planet. Change* **2013**, *108*, 119−127.
(96) Ariya, P. A.; Amyot, M.; Dastoor, A.; Deeds, D.; Feinberg, A.; Kos, G.; Poulain, A.; Ryjkov, A.; Semeniuk, K.; Subir, M.; Toyota, K. Mercury Physicochemical and Biogeochemical Transformation in the Atmosphere and at Atmospheric Interfaces: A Review and Future Directions. *Chem. Rev.* **2015**, *115*, 3760−3802.
(97) Alexander, M.; Scott, J. The Influence of ENSO on Air-Sea Interaction in the Atlantic. *Geophys. Res. Lett.* **2002**, *29*, 46-1−46-4.
(98) Enfield, D. B.; Mayer, D. A. Tropical Atlantic Sea Surface Temperature Variability and Its Relation to El Niño-Southern Oscillation. *J. Geophys. Res.: Planets* **1997**, *102*, 929−945.
(99) Su, H.; Neelin, J. D.; Meyerson, J. E. Mechanisms for Lagged Atmospheric Response to ENSO SST Forcing. *J. Clim.* **2005**, *18*, 4195−4215.

https://doi.org/10.1021/acs.est.1c00691
Environ. Sci. Technol. 2021, 55, 7145−7156